RSC Advances

PAPER

Insights into solvent vapor annealing on the performance of bulk heterojunction solar cells by a quantitative nanomorphology study

Cite this: *RSC Adv.*, 2014, **4**, 6246

H.-C. Liao,[a] C.-S. Tsao,*[b] Y.-C. Huang,[b] M.-H. Jao,[a] K.-Y. Tien,[a] C.-M. Chuang,[b] C.-Y. Chen,[b] C.-J. Su,[c] U.-S. Jeng,[c] Y.-F. Chen[d] and W.-F. Su*[a]

Received 6th October 2013
Accepted 12th November 2013

DOI: 10.1039/c3ra45619f

www.rsc.org/advances

Bulk heterojunctions (BHJ) represent the most promising structures for high efficiency polymer solar cells and their morphologies can be finely tuned by post-treatments such as thermal annealing and solvent vapor annealing. Though extensive studies have shown improved power conversion efficiencies by tuning the treating parameters of both treatments, substantial knowledge of how the BHJ morphologies evolve with various solvent vapors related to photovoltaic characteristics and differ from those with thermal annealing is still limited. Herein we employed simultaneous grazing incidence wide and small angle X-ray scattering (GIWAXS/GISAXS) to systematically investigate the changes in morphology of a poly(3-hexylthiophene)/C61-butyric acid methyl ester (P3HT–PCBM) BHJ manipulated by solvent vapor annealing using different solvents. Solvents with different solubility, *i.e.* non-solvent, poor solvent and good solvent were studied. Distinctive morphologies were quantitatively resolved among these solvent vapor-annealed BHJs and their evolutions during processing are interpreted. The resolved morphologies can clearly explain the subtle variations in photovoltaic characteristics of open circuit voltage (V_{oc}), short circuit current (J_{sc}) and fill factor (FF) related to the working mechanism of the BHJ, *i.e.* carrier generation, carrier transportation and recombination. This work provides fundamental new insights into how the BHJ morphologies and photovoltaic characteristics can be flexibly tailored by solvent vapor annealing using various kinds of solvent vapors.

Introduction

Polymer solar cells have attracted considerable attention in the last decade due to the advantages of light weight, solution processibility, flexibility, semi-transparency, low cost, *etc.* An improved power conversion efficiency (PCE) critically relies on the phase-separated morphology of the bulk heterojunction (BHJ) in which the self-organized electron donor (polymer) and aggregated electron acceptor clusters form bicontinuous phases. The PCE can be enhanced by manipulating the BHJ nanomorphology through thermal annealing,[1–7] solvent vapor annealing,[1,5,8–12] processing additives' incorporation,[13–19] *etc.* The first two treatments are called post-treatment whereby the BHJ films are processed after being cast. They enable control over the self-organized BHJ morphologies by finely tuning the treating conditions or parameters. Stepwise thermal annealing of the poly-3-hexylthiophene–[6,6]-phenyl-C_{61}-butyric acid methyl ester (P3HT–PCBM) BHJ was extensively reported to well tune the phase-separated morphologies giving improved PCEs.[20] Similarly, solvent vapor annealing has been widely adopted as it is a milder post-treatment compared with thermal annealing.[1,5,8–12] Park *et al.* compared the difference in solar cell performance between good-solvent annealing and poor-solvent annealing.[8] Both thermal annealing and solvent vapor annealing have been shown to improve PCEs, however, substantial knowledge of how BHJs treated by different solvent vapor annealing techniques differ, as well as comparing with those treated by thermal annealing with regards to the distinctive evolution of their morphology, *i.e.* mechanistic behavior, is limited. Furthermore, the variation of photovoltaic characteristics, *i.e.* open circuit voltage (V_{oc}), short-circuit current density (J_{sc}), and fill factor (FF) depends on different thermally tuned and solvent vapor-tuned BHJ morphologies.[5,8,10] To date, few studies quantitatively correlate the hierarchical BHJ morphology tailored by different solvent vapor annealing processes to the associated performances for the explanation of device working mechanisms (*i.e.*, exciton dissociation, mobile carrier generation and recombination). Transmission electron

[a]*Department of Materials Science and Engineering, National Taiwan University, Taipei 10617, Taiwan. E-mail: suwf@ntu.edu.tw; Fax: +886 2 33664078; Tel: +886 2 33664078*

[b]*Institute of Nuclear Energy Research, No. 1000, Wenhua Road, Longtan Township, Taoyuan County 32546, Taiwan. E-mail: cstsao@iner.gov.tw; Tel: +886 3 4711400 ext. 3420*

[c]*National Synchrotron Radiation Research Center, No. 101, Hsin-An Road, Hsinchu 300-77, Taiwan*

[d]*Department of Physics, National Taiwan University, No. 1, Sec. 4, Roosevelt Road, Taipei 10617, Taiwan*

microscopy (TEM) or atomic force microscopy (AFM) can only provide local and qualitative information (P3HT-rich and PCBM-rich domains) due to some inherent limitations. Simultaneous grazing incidence wide- and small-angle X-ray scattering (GIWAXS/GISAXS) has shown to be a powerful technique in the quantitative structural characterization of BHJ in different length scales for thin films.[20–27] This technique becomes a necessary tool to complement conventional microscopic studies. Verploegen *et al.* investigated solvent vapor annealing effects using the powerful time-resolved GIWAXS techniques.[28] Their work provides informative morphological evolutions and mechanisms of P3HT–PCBM BHJ films before, during and after solvent vapor annealing. More insights into the quantitative correlations among solvent vapor annealing effects, multi-length scale structures in BHJ films, and photovoltaic characteristics are necessary. Moreover, guidance for selecting solvent vapors with different solubilities and interactions with BHJ films are necessary toward rational process designs of a high efficiency device.

In our previous work, we demonstrated an improved GISAXS model analysis for a P3HT–PCBM BHJ as a quantitative structural characterization method for evaluating the self-organized morphologies.[20] It is essential to investigate solvent annealing by the study of the correlation between solvent vapor-tuned BHJ morphologies and subtle variations of the photovoltaic characteristics. In the present work, we compare a solvent-annealed P3HT–PCBM BHJ using three solvent vapors *i.e.* methanol (MeOH), *o*-xylene (xylene), and dichlorobenzene (DCB). P3HT and PCBM exhibit substantially different solubilities in the solvents, which is the most crucial factor in the morphological manipulation. The thermally annealed (TA) P3HT–PCBM BHJ is also included for a comprehensive comparison. The simultaneous GIWAXS/GISAXS technique was employed to systematically investigate the morphologies of phase-separated P3HT and PCBM domains on different length scales tuned by these post-treatments. We provide new insights that the BHJ structural evolutions due to these post-treatments can be distinctive. The relationship between the treating parameters (due to the different solvent solubility for P3HT and PCBM) and the corresponding evolution of morphologies is explored with respect to (1) the crystallization of the self-organized P3HT phase, (2) the nanoscale PCBM clusters aggregated by the diffusion of PCBM molecules, (3) the domain size and spatial distribution of mesoscale amorphous P3HT chains intercalated with PCBM molecules (also called the PCBM–amorphous P3HT domain) and (4) the spatial arrangement of P3HT crystallites and PCBM aggregated clusters in the bicontinuous phase. Moreover, the corresponding photovoltaic characteristics regarding V_{oc}, J_{sc} and FF correlated to the resolved BHJ morphologies are presented here. The related mechanism is also discussed in terms of exciton dissociation, mobile carrier generation and recombination. The demonstrated results provide new insights into how the BHJ nanomorphology and photovoltaic properties can be finely tailored by solvent vapor annealing using solvent vapors in which the various solubilities are different. They can be further extended to other BHJ systems and serve as a guide for the processing design of solvent vapor annealing.

Experimental section

Device fabrication and performance measurement

The P3HT–PCBM blend solution was prepared by dissolving 10 mg P3HT (Rieke Metals, Inc. 4002E) and 8 mg PCBM (Nano-C, Inc.) in 1 ml chlorobenzene and stirred at 40 °C for two days. The solar cell devices were fabricated by layer-by-layer deposition. The patterned (2 mm × 10 mm stripe) transparent electrode indium tin oxide (15 ohms per square, Luminescence Technology Corp.) was ultrasonically cleaned by a series of solvents (ammonia–H_2O_2–deionized water, methanol, isopropanol) and then treated by oxygen plasma. A thin hole transporting layer (40 nm) PEDOT:PSS (Baytron P 4083) was spin coated on the top of the electrode. The substrates were then transferred into a glove box filled with nitrogen for the following processing (with concentrations of oxygen and water lower than 0.1 ppm). Afterwards, the P3HT–PCBM BHJ was deposited by spin coating at 700 rpm for 1 minute which resulted in a thickness of ~80 nm. For the solvent vapor annealing process, the as-cast P3HT–PCBM films were reversely stuck on the lids of Petri dishes which were filled with liquid solvents of methanol, *o*-xylene, and dichlorobenzene for an hour. The thermal annealing was carried out by annealing the as-cast film at 130 °C for 10 minutes. Finally, 40 nm Ca and 100 nm Al (3 mm × 10 mm stripe perpendicular to the ITO stripe) were thermally evaporated under vacuum at 3×10^{-6} torr to complete the solar cell fabrication, leading to a crossbar active area of 0.06 cm^2. The photocurrent–voltage curves were characterized by a Keithley 2400 source meter under air mass (A.M.) 1.5 radiation (100 mW cm^{-2}) from a solar simulator source (Newport Inc.). Ten independently fabricated devices were measured for each processing strategy for obtaining the statistics/uncertainty of the device performances.

GIWAXS/GISAXS structural characterization

The GIWAXS/GISAXS measurements were performed at beamline 23A of NSRRC, Taiwan. For sample preparation, the P3HT–PCBM BHJs were deposited on silicon substrates and the subsequent thermal and solvent vapor annealing treatments corresponding to the solar cell devices were performed. The scattering effects of the PEDOT:PSS layer and background due to the substrate on the analysis of BHJ morphologies have been discussed in our previous work and can be ignored.[29] The thin films were characterized by a monochromated X-ray beam (8 keV, wavelength $\lambda = 1.55$ Å, incidence angle = 0.2°). The two dimensional (2-D) GIWAXS and GISAXS patterns were simultaneously collected by a CMOS flat panel X-ray detector (C9728DK, 52.8 mm square, situated 7.2 cm from the sample) and a CCD detector (MAR165, 165 mm in diameter, 1024 by 1024 pixels resolution, situated 309.5 cm from sample), respectively. The details of the instrumental configuration, operation and data reduction procedures of the GISAXS/GIWAXS measurement are described elsewhere.[20,23] The reduced 1-D GIWAXS profiles were obtained by integrating along the out-of-plane direction (defined as the Q_z direction) normal to the film surface and the in-plane direction (defined as Q_x direction) parallel to the film

surface. The 1-D GISAXS profiles were reduced by integrating the 2-D patterns along the in-plane direction.

Results and discussion

Analysis of GIWAXS and GISAXS results

The as-cast and thermally annealed BHJ are denoted as CAST and TA, respectively. The P3HT–PCBM BHJs annealed by solvent vapors of methanol, *o*-xylene, and dichlorobenzene are denoted as SA_MeOH, SA_Xylene and SA_DCB, respectively. The solubility of P3HT and PCBM in these solvents was quantitatively determined by adding an excess amount of solutes into each solvent, centrifuging out the insoluble solutes from the solution, weighing out the insoluble portion and then calculating the soluble solutes. DCB shows the highest solubility to both P3HT and PCBM with 37 mg ml^{-1} and 27 mg ml^{-1}, respectively. In contrast, MeOH is completely unable to dissolve either P3HT or PCBM. The solubilities in xylene were 0.5 mg ml^{-1} and 6.1 mg ml^{-1} for P3HT and PCBM, respectively, which lie between the values with DCB and MeOH. Therefore, DCB, xylene and MeOH are classified as good-solvent, poor-solvent and non-solvent, respectively, for both P3HT and PCBM. The representative 2-D GIWAXS pattern of the CAST film is shown in Fig. 1(a). The diffraction spot at $Q = 0.38$ $Å^{-1}$ arises from the (100) lamellar planes of oriented P3HT crystallites with a spacing of 16.5 Å. Fig. 1(b) and (c) show the reduced 1-D out-of-plane and in-plane GIWAXS profiles, showing (100) diffraction peaks primarily contributed by edge-on crystallites (oriented with the lamellar plane parallel to the film surface) and face-on crystallites (lamellar plane normal to the film surface), respectively, for the CAST, SA_MeOH, SA_Xylene, SA_DCB and TA BHJ films. Generally, the scattering intensities of the (100) lamellar plane of the edge-on crystallites (Fig. 1(b)) is nearly an order of magnitude larger than those of the face-on crystallites for all films. The results are consistent with our previous work that the (100) lamellar planes are preferentially orientated parallel to the substrates, *i.e.* edge-on type P3HT crystallites.[24] Herein we defined the integration of the (100) scattering peak in Fig. 1(b) as the partial relative crystallinity (PRC) contributed from edge-on crystallites. Note that it can be observed that the (100) scattering peaks reveal extended arcs, which indicate that some of the crystallites are orientated with a small tilt angle relative to the exact edge-on crystallites, *i.e.* there is a spread of the crystal orientation. In the present work we also classified these crystallites as the edge-on crystallites. In order to compare the partial crystallinities of the edge-on crystallites among all the sample films, the range of the integration was determined to be capable of covering the arcs for all of the BHJ films. Therefore, almost all the edge-on type crystallites (though most of them are not exactly edge-on) are included when the 2-D GIWAXS patterns were reduced to 1-D GIWAXS profiles. The PRC values are summarized in Table 1 based on the normalization to that of the TA film. For the P3HT–PCBM BHJ annealed by MeOH vapor (SA_MeOH), the PRC is similar to that of the CAST film, which is without almost any face-on type crystallites (Fig. 1(c)). On the contrary, the SA_Xylene, SA_DCB and TA BHJ films reveal a significant increase in PRC for edge-on crystallites and a smaller increase in face-on type crystallites compared with the CAST film. The domain size of the edge-on crystallites can be approximated according to the Scherrer equation $D_i = 2\pi/\Delta Q$, i represents either X or Z orientation, where ΔQ is the full width at half maximum, as summarized in Table 1.

The in-plane GISAXS profiles of the BHJ films are shown in Fig. 2. These GISAXS intensities can be model fitted by our previous SAXS model,[20] comprised of the Debye–Anderson–Brumberger equation (so-called DAB model)[30] and the polydispersed hard-sphere model[29] as given by

$$I(Q) = I_{\mathrm{DAB}}(Q) + I_{\mathrm{HS}}(Q) + b \quad (1)$$

where $I_{\mathrm{DAB}}(Q)$ is the intensity calculated by the DAB model. It dominates the intensity in the low-Q region with a power-law scattering behavior, showing an upturn in the Q range of 0.005–0.015 $Å^{-1}$. The parameter "characteristic length (ξ)" can be extracted from the DAB equation. It roughly describes the size of

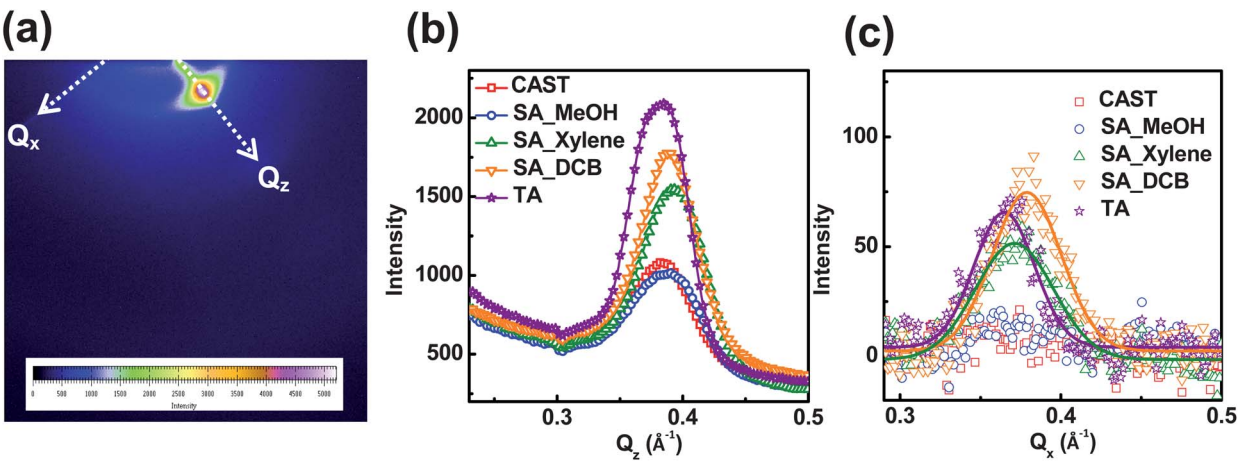

Fig. 1 (a) 2-D GIWAXS patterns of the CAST film. (b) Out-of plane and (c) in-plane 1-D GIWAXS profiles of as-cast P3HT–PCBM BHJ film and P3HT–PCBM BHJ films with solvent annealing by MeOH, xylene and DCB, and thermal annealing at 130 °C for 10 min (*i.e.*, CAST, SA_MeOH, SA_Xylene, SA_DCB and TA films, respectively) reduced along the out-of-plane direction and the in-plane directions, respectively.

Table 1 Structural parameters determined by GIWAXS/GISAXS results, model fitted GISAXS intensities, and associated solar cell characteristics with respect to different BHJ films. The maximum PCEs of the solar cell devices based on these thin films are also listed. The PCE values show the best-performing device PCEs and the average PCEs with PCE distribution (standard deviation) in parentheses obtained from 10 devices

Thin films	PRC	$D_{z(100)}$ (nm)	η (%)	R (nm)	ξ (nm)	S_v ($\times 10^{-3}$) (Å^{-1})	$S_v/(\eta/R)$	V_{oc} (volts)	J_{sc} (mA cm^{-2})	FF	PCE (%)
CAST	0.66	9.1	2.4	4.4	35	2.2	4.0	0.70	5.6	0.41	1.61 (1.47 ± 0.11)
SA_MeOH	0.62	8.1	2.5	4.5	35	2.2	3.9	0.67	5.2	0.41	1.43 (1.31 ± 0.12)
SA_Xylene	0.87	9.2	12.9	6.3	22	7.4	3.6	0.58	9.7	0.51	2.87 (2.62 ± 0.10)
SA_DCB	0.82	11.0	14.0	6.3	18	6.2	2.7	0.62	9.5	0.60	3.53 (3.41 ± 0.08)
TA	1	11.2	19.0	8.7	18	6.1	2.8	0.64	9.7	0.61	3.79 (3.71 ± 0.07)

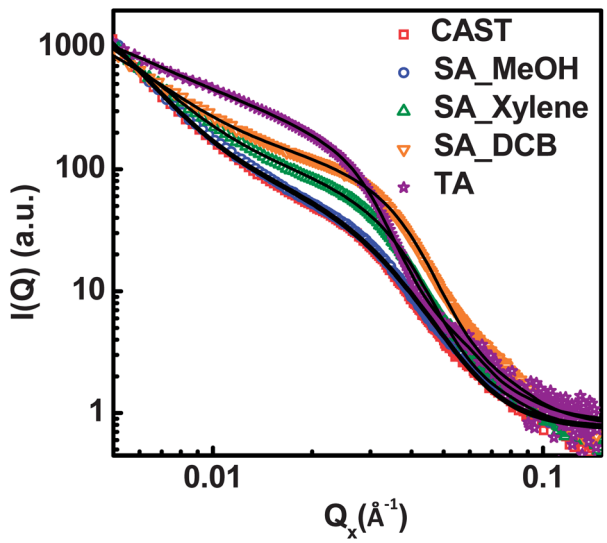

Fig. 2 GISAXS profiles of the as-cast P3HT–PCBM BHJ film and P3HT–PCM BHJ films with solvent annealing by MeOH, xylene and DCB, and thermal annealing at 130 °C for 10 min, (*i.e.*, CAST, SA_MeOH, SA_Xylene, SA_DCB and TA films, respectively). The solid lines are calculated by model fitting.

the large-scale amorphous P3HT intercalated with PCBM molecules (denoted as PCBM–amorphous P3HT domains) without ordered structures. The $I_{HS}(Q)$ is the intensity calculated by polydispersed hard-sphere model. It contributes in the middle- and high-Q range (0.02–0.07 Å^{-1}) with a shoulder, revealing the interaction between PCBM cluster (like an ordering peak to a certain extent). The shoulder is in terms of the product of the form factor of PCBM clusters (related to cluster radius (R)) and structure peak (inter-particle effect, related to cluster radius (R), volume fraction (η), and polydispersity of size distribution (P)).[31] The constant b is due to incoherent scattering background. The GISAXS profiles of all films can be fitted well using eqn (1) and the obtained structural parameters are summarized in Table 1.

Effect of post-treatment type on the evolution of BHJ morphologies

According to the GIWAXS and GISAXS results (Fig. 1 and Table 1), the thermal annealing and solvent vapor annealing by three different kinds of solvent vapors result in distinctively different crystallization behaviors of P3HT. The SA_MeOH film reveals an almost unchanged P3HT crystal size, similar PRC and characteristic length to those of the CAST film, which can be attributed to the P3HT being insoluble in MeOH vapor. In contrast, the xylene vapor-, DCB vapor- and thermally annealed BHJ reveal significantly enhanced PRCs compared with the CAST film. This suggests that these three treatments lead to the transformation of amorphous P3HT into ordered lamellar structures. Nevertheless, the corresponding crystallization behaviors are found to be different as indicated by the structural parameters (Table 1). For the thermally annealed BHJ (TA), the D_z is increased from 9.1 nm (the CAST film) to 11.2 nm.

Additionally, the domain size of the PCBM–amorphous P3HT domains (*i.e.* characteristic length) decreases considerably from 35 nm to 18 nm after thermal annealing. According to the literature,[32,33] two types of P3HT crystallization behavior evolve during thermal annealing: (1) the growth of originally existing crystallites and (2) the formation of new crystallites nucleated and transformed from the local region of the PCBM–amorphous P3HT domains. The newly organized crystallites in (2) spatially distribute within the PCBM–amorphous P3HT domains and thus the characteristic lengths of the new domains are reduced.

The characteristic lengths in the TA, SA_DCB and SA_Xylene blend films are similar. However, the crystallization behaviors induced by solvent vapor annealing are different from those by thermal annealing (*cf.* Table 1). Herein, combining our GIWAXS results with those of Verploegen,[28] we propose a mechanistic interpretation of the morphological evolution of BHJ films during solvent vapor annealing and also compare the crystallization behaviors of xylene- and DCB-annealed BHJ films. The evolution can be interpreted with respect to the early stage and latter stage of solvent vapor annealing as shown in Fig. 3. The P3HT crystal size increased in the early stages of solvent vapor annealing, which can be attributed to the transformation of amorphous P3HT chains (*i.e.* PCBM–amorphous P3HT domains) into crystallites or an increase in paracrystalline order. The different solubility in the solvent vapors would lead to different conformations of amorphous mobile P3HT chains during solvent vapor annealing and hence different crystal sizes and number of crystallites (*i.e.*, crystallinity). Due to the high solubility of P3HT in DCB (36 mg ml^{-1}), the amorphous P3HT would be significantly swelled by the DCB vapors, thus the strong interaction between the P3HT and solvent molecules drive the P3HT chains to stretch out. The extending P3HT chains would favor the formation of larger P3HT crystallites

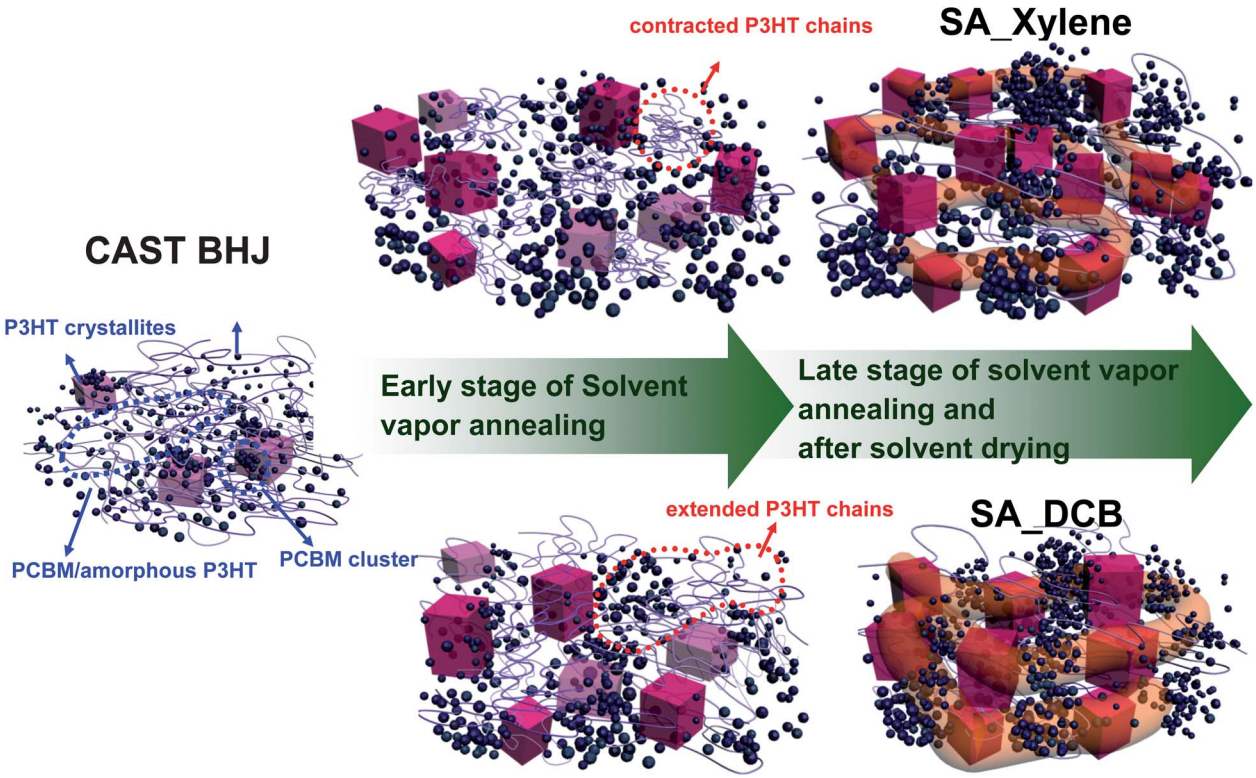

Fig. 3 Schematic of the morphological evolutions of P3HT–PCBM BHJs influenced by xylene and DCB vapors. The P3HT–PCBM blends reveal different P3HT conformations (small contracted chains in xylene vapor and large extended chains in DCB vapor) during the early stages of solvent vapor annealing and hence different morphologies of P3HT crystallites (smaller size and larger number for the SA_Xylene film than for SA_DCB). The spatially separated P3HT crystallites and PCBM aggregated clusters are shown in the SA_Xylene BHJ blend; the inter-connection of P3HT crystallites and PCBM aggregated clusters are also shown in the SA_DCB blend. Herein we illustrate the fibrous microstructures of P3HT in the late stages of the morphological evolution.

(~11.0 nm) during the early stages of solvent vapor annealing, as illustrated in Fig. 3. In contrast, the much lower solubility in xylene (0.5 mg ml^{-1}) would lead to the P3HT chains contracting during solvent vapor annealing and thus give rise to smaller crystallites (~9.2 nm) in the SA_Xylene BHJ film (illustrated in Fig. 3). The poor solubility would also facilitate the precipitation and/or nucleation of P3HT crystallites from the PCBM–amorphous P3HT domains and thus give rise to a larger amount of P3HT crystallites in the SA_Xylene BHJ film. The distinctive crystallization behaviors of P3HT influenced by solvent vapor annealing with different solubility are proposed herein and schematically shown in Fig. 3. The crystallization tailored by solvent vapor would be relatively quick and immediately remain stable in the course of solvent vapor annealing (*i.e.* during the later stage of solvent vapor annealing and after solvent drying, Fig. 3). It is noteworthy that the microstructure of P3HT crystallites is regarded as nanofibers connected by crystallites in which the P3HT chains fold into a lamellar structure in a cubic shape.[22] Herein we illustrate the fibrous structures in the late stage of morphological evolution.

The crystallization behavior of P3HT influences the structural evolution of PCBM. The volume fraction of the PCBM clusters formed by the aggregation of molecules in the CAST and SA_MeOH films is relatively low ($R \sim 4.5$ nm, $\eta \sim 2.5\%$), which implies that most of the PCBM molecules are spatially dispersed around the polymer chains with little aggregation. When the solvent vapor (xylene or DCB) was introduced, the PCBM molecules intercalated with amorphous P3HT were excluded from the transformation of amorphous P3HT into lamellar crystallites. This led to the aggregation of PCBM molecules into PCBM clusters ($R \sim 6$ nm and $\eta \sim 12.9$–14.0%) surrounding the P3HT crystallites (Fig. 3). Such driving force from the organization of P3HT is distinctive to the thermal diffusion in the thermal annealing process which reveals the largest PCBM cluster size of $R \sim 8.7$ nm and the highest volume fraction of 19.0%. It suggests that the thermally driven diffusion results in a larger degree of phase separation between P3HT and PCBM compared with solvent vapor annealing. Additionally, we employed the previously established index, specific surface area (S_v) (as shown in Table 1),[20] to evaluate the surface area between the aggregated PCBM clusters and the surrounding matrix. Briefly, for the PCBM cluster with a sharp cluster–matrix interface, the GISAXS profiles reveal an asymptotic behavior in the high-Q region, where $I(Q) \propto Q^{-4}$. The specific interface area S_v (defined as the surface area of the PCBM clusters per unit volume) can be determined independently by the Porod approximation given by Glatter *et al.*[34] The S_v value is an important structural parameter in correlation with photovoltaic properties. According to the working mechanism of a BHJ solar cell device, the interfaces between donors (P3HT) and acceptors

(PCBM) are critical for efficient exciton dissociation. The total interface areas were simultaneously contributed to by PCBM molecules (dispersed in amorphous P3HT chains) and PCBM clusters (surrounding P3HT crystallites) with P3HT phases. However, the carriers which are dissociated at the former-type interfaces would have little opportunity to generate a useful photocurrent because of the discontinuous pathway for carrier transport. The elaboration of S_v mainly takes the interfaces contributed to by PCBM clusters into account, at which the exciton dissociation is more efficient. Furthermore, we also determined the partial attachment of spatially distributed PCBM clusters by the value $S_v/(\eta/R)$.[20] From Table 1, the SA_Xylene, SA_DCB and TA films show remarkably increased S_v values compared with the CAST and SA_MeOH films owing to the diffusion of PCBM into a large volume fraction of aggregated clusters. Nevertheless, the spatial distributions of the PCBM clusters are found to be different between the SA_Xylene and SA_DCB films as signified by the index $S_v/(\eta/R)$ (Table 1). The smaller value of $S_v/(\eta/R)$ indicates that greater partial attachment between the PCBM clusters leads to the formation of large-scale agglomerations.[20] Interestingly, the xylene vapor-annealed BHJ reveals separated clusters but the DCB vapor-annealed BHJ shows substantial agglomerations from partially connected PCBM clusters. It can be speculated that a large number of contracted P3HT chains are distributed around the PCBM-rich domains during xylene vapor annealing. Consequently, the PCBM-rich domains aggregate into PCBM clusters with few interconnections between clusters due to the interruption of the surrounding P3HT crystallites after xylene drying. The spatial distribution of the PCBM clusters are crucial to the resultant photovoltaic characteristics as discussed in the following section.

Correlation between BHJ morphologies and photovoltaic characteristics

Fig. 4 shows the photocurrent–voltage (J–V) curves of the photovoltaic devices based on the BHJs with different post-treatments. The corresponding photovoltaic characteristics of V_{oc}, J_{sc}, FF and PCE are summarized in Table 1. The devices with the CAST and SA_MeOH BHJs exhibit low PCEs of 1.61% and 1.43%, respectively, mainly because of the low J_{sc} and FF. These two devices, however, have the highest V_{oc} of 0.67–0.70 volts (discussed later). After the BHJs were post-treated by thermal annealing or solvent vapor annealing using xylene or DCB, the devices show considerably improved J_{sc} of ~9.5 mA cm^{-2}, higher than that of the CAST BHJ by nearly two times. Additionally, the FF values of the SA_Xylene, SA_DCB, and TA BHJ solar cells are also remarkably increased to 0.51, 0.60 and 0.61, respectively. However, compared with that of the CAST device, a reduction of the V_{oc} is observed in these three post-treated BHJ solar cells with a decrease of 0.12, 0.08 and 0.06 volts, respectively. Notably the SA_Xylene BHJ device shows the largest drop of V_{oc} (V_{oc} ~ 0.58 volts) relative to the CAST device (discussed later). We conclude that the overall PCE increased from 1.6% to 2.9%, 3.5% and 3.8% after post-treatments of xylene vapor annealing, DCB vapor annealing and thermal annealing, respectively.

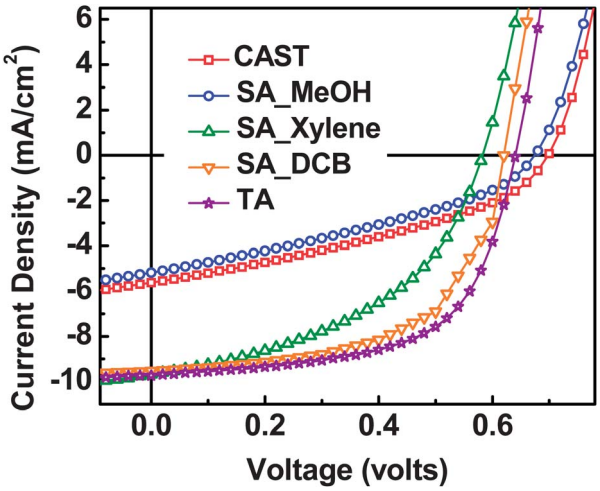

Fig. 4 Photocurrent–voltage curves of the solar cells device based on as-cast P3HT–PCBM BHJ blends and P3HT–PCBM BHJ blends with solvent annealing by MeOH, xylene and DCB, and thermal annealing at 130 °C for 10 min, (*i.e.*, CAST, SA_MeOH, SA_Xylene, SA_DCB and TA films, respectively).

It has been reported that films cast from chloroform revealed a more favorable P3HT orientation for charge transport (*i.e.* face-on type crystallites with π–π stacking perpendicular to the substrates) than those cast from chlorobenzene.[28] Additionally, the authors further stated that chlorobenzene led to a BHJ morphology which was less susceptible to morphological manipulation and device performance improvements compared with chloroform.[28] Herein our work differently demonstrates the interesting results that a BHJ morphology cast from chlorobenzene can be substantially manipulated by different treatments according to the significantly improved device performances correlated to the various scales of the nanostructures. Furthermore, the P3HT crystallites in the BHJ films reported in our work are mainly of the edge-on type (with the alkyl chain perpendicular to the substrate), which generally is not the favorable orientation for charge transport, but the corresponding devices exhibited high efficiencies of 3.5–3.8%, which are close to the values reported in the references.[1,3–5] Therefore, our distinctive results (device performances correlating to GIWAXS/GIWAXS characterizations) imply that the orientation of the P3HT crystallites is not a critical factor when determining the PCEs. The other structural information shown in Table 1 plays a more important role as discussed in the following paragraphs.

We tried to correlate the photovoltaic characteristics quantitatively with the resolved structural parameters of the BHJs based on the working mechanism of solar cells. In the CAST and SA_MeOH BHJ films, a large fraction of PCBM molecules are intercalated within the P3HT amorphous regions and spatially separated from each other. This molecule-scale dispersion should provide large P3HT–PCBM interface areas but has difficulties in providing enough domain size for the dissociated electron and hole to diffuse apart. As a result, the dissociated electron–hole pairs without a sufficiently separated distance would have a high probability of undergoing back

recombination (so-called geminate recombination) due to a mutual electrostatic force (illustrated in Fig. 5(a)). Discernible geminate recombination could account for the relatively low yields of useful current and thus a lower J_{sc} (~5.6 mA cm^{-2}) and FF (~0.41) compared with other solar cells. In contrast, the devices with SA_Xylene, SA_DCB and TA films show remarkably improved J_{sc} (~9.5 mA cm^{-2}) and FF (0.51–0.60), which could be correlated to the large volume fraction of phase-separated domains, *i.e.* aggregated PCBM clusters (~12 nm) and self-organized P3HT crystallites (~10 nm), for dissociated carriers diffusing out of the P3HT–PCBM interfaces. The S_v would hence be an informative index to evaluate the efficient exciton dissociation. Namely, the total interface areas between P3HT–PCBM were simultaneously contributed to by PCBM molecules and PCBM clusters (aggregated from PCBM molecules) with P3HT phases. According to the elaboration of S_v,[20] it mainly takes the interfaces contributed to by PCBM clusters into account at which the exciton dissociation is more efficient. Therefore, the S_v index can signify the "effective surface area" for efficient exciton dissociation. The improved J_{sc} and FF influenced by thermal annealing, xylene or DCB solvent vapors can be correlated with the significantly increased S_v values (increased three-fold from 2.2 × 10^{-3} Å^{-1} to 6–7 × 10^{-3} Å^{-1}) compared with those of the CAST and SA_MeOH films.

We are interested in the SA_Xylene, SA_DCB and TA BHJ films which reveal similar J_{sc} values but subtle variations in V_{oc} and FF. In addition to the efficient exciton dissociation, the generation of output photocurrent also critically relies on free carrier transport. Morphology with bicontinuous phases could facilitate the carrier transport toward electrodes. In our present work, the phase-separated domains generally possess sizes near 10–15 nm. Considering the BHJ film thickness is around 150 nm–200 nm, the interconnection between the domains is crucial for efficient carrier transport. We tried to correlate the carrier transport with the domain connections by the structural parameters of D_z and $S_v/(\eta/R)$ for the P3HT phase and PCBM phase, respectively. Namely, a larger D_z with a higher possibility of crystallite connection would reduce the gaps between crystallites and would also reduce insufficient carrier transport by hopping. Similarly, the smaller index of $S_v/(\eta/R)$ also signifies that more partially connected PCBM clusters form continuous agglomerations, which would also prevent the loss during carrier transport as we illustrated in Fig. 5(b). Therefore, according to Table 1, the SA_Xylene BHJ shows a smaller crystal size (D_z = 9.2 nm) than those of the SA_DCB and TA films (D_z ~ 11 nm). Additionally, the calculated $S_v/(\eta/R)$ value of SA_Xylene BHJ is much larger than those of the SA_DCB and TA films. Both of the structural characteristics could account for the smaller FF of 0.51 in the SA_Xylene device compared with those of the SA_DCB (FF = 0.60) and TA (FF = 0.61) films.

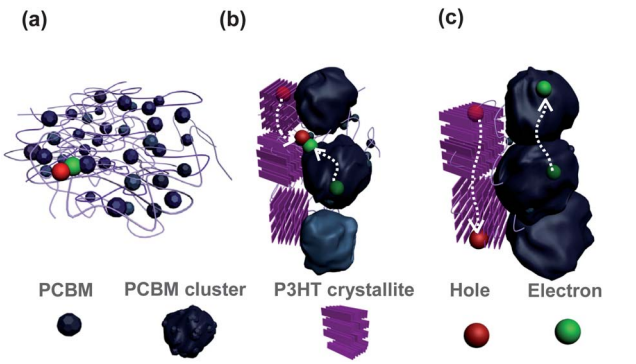

Fig. 5 Illustrations of the P3HT–PCBM BHJ morphologies annealed by solvent vapors with different solubility. (a) The SA_MeOH BHJ reveals spatially dispersed PCBM molecules within amorphous P3HT chains which leads to a discernible recombination of electron–hole pairs (excitons) due to electrostatic attraction. (b) The SA_Xylene BHJ shows phase-separated P3HT crystallites and PCBM clusters but few connections in between. (c) The SA_DCB BHJ film exhibits efficient morphology with bicontinuous phases of interconnected P3HT crystallites and PCBM clusters which respectively correlates with efficient carrier generation and transport.

The V_{oc} is also of interest because it covers a wide range (from 0.70 to 0.58 volts). The output voltage can be affected by the energy level of the donor materials and acceptor materials, with the theoretical V_{oc} being related to the energy difference between the highest occupied molecular orbital (HOMO) of P3HT and the lowest unoccupied molecular orbital (LUMO) of PCBM. The drop of V_{oc} from 0.7 volts for the CAST film to 0.58–0.64 volts for the SA_Xylene, SA_DCB and TA films could be correlated with the sizes of the phase-separated domains of P3HT and PCBM. Specifically speaking, the higher crystallinity and larger PCBM domain size (PCBM clusters) in the SA_Xylene, SA_DCB and TA films in comparison with the CAST film mean they possess more delocalized electrons, and thus the energy band gaps of both P3HT and PCBM are reduced. Consequently, the energy difference between the HOMO of P3HT and the LUMO of PCBM is reduced, leading to the decreased V_{oc}. Regarding the SA_Xylene, SA_DCB and TA devices, they reveal differences of V_{oc} ranging from 0.58 volts to 0.64 volts. It was recently evidenced that non-geminate recombination loss (recombination of free carriers during transport) has an significant impact on the reduction of V_{oc}.[35] Therefore, it can be correlated to the present work that the SA_Xylene BHJ film with smaller D_z, larger $S_v/(\eta/R)$ (Table 1) and higher possibility of loss during free carrier transport (less interconnection of P3HT and PCBM domains, Fig. 5(b)) would give rise to a lower V_{oc} compared with the SA_DCB and TA devices. In conclusion, tailoring the V_{oc} in BHJ solar cells critically depends on the phase-separated domains and their interconnections for efficient carrier transport. The thermal and DCB vapor annealing show the least reduced V_{oc} when the phase-separated nanomorphology significantly improves the J_{sc} and FF as illustrated in Fig. 5(c) for an efficient BHJ morphology.

Conclusions

In summary, we demonstrate different BHJ morphologies and morphological evaluations of P3HT–PCBM BHJ film treated by thermal and solvent vapor annealing. The solubility of the film in the solvent (non-solvent, poor solvent and good solvent) critically affects the conformation of P3HT and distribution of the PCBM-rich domains during solvent vapor annealing, and also impacts the resultant morphologies of the BHJ films after

solvent drying, *i.e.* self-organized P3HT crystallites, spatially distributed PCBM–amorphous P3HT domains, aggregated PCBM clusters, and agglomerations of interconnected PCBM clusters. These solvent vapor-tuned morphologies can be correlated with the subtly varied photovoltaic characteristics in terms of V_{oc}, J_{sc} and FF on the working mechanism basis of carrier generation, carrier transportation, and recombination loss. The present study demonstrates the valuable correlations among BHJ morphologies, photovoltaic properties, and solvent vapor annealing with different solubilities which can guide associated processing designs toward an optimized BHJ morphology and high efficiency solar cells.

Acknowledgements

Financial support obtained from the National Science Council of Taiwan (100-2120-M-002-007 and 100-3113-E-002-012) and the Institute of Nuclear Energy Research (Projects 10120011NER030) is highly appreciated.

Notes and references

1 G. Li, V. Shrotriya, J. Huang, Y. Yao, T. Moriarty, K. Emery and Y. Yang, *Nat. Mater.*, 2005, **4**, 864–868.
2 W. Ma, C. Yang, X. Gong, K. Lee and A. J. Heeger, *Adv. Funct. Mater.*, 2005, **15**, 1617–1622.
3 Y. Kim, S. Cook, S. M. Tuladhar, S. A. Choulis, J. Nelson, J. R. Durrant, D. D. C. Bradley, M. Giles, I. McCulloch, C. Ha and M. Ree, *Nat. Mater.*, 2006, **5**, 197–203.
4 J. L. Wu, F. C. Chen, Y. S. Hsiao, F. C. Chien, P. Chen, C. H. Kuo, M. H. Huang and C. S. Hsu, *ACS Nano*, 2011, **5**, 959–967.
5 S. S. V. Bavel, E. Sourty, G. D. With and J. Loos, *Nano Lett.*, 2009, **9**, 507–513.
6 B. Y. Yu, W. C. Lin, W. B. Wang, S. I. Iida, S. Z. Chen, C. Y. Liu, C. H. Kuo, S. H. Lee, W. L. Kao, G. J. Yen, W. W. You, C. P. Liu, J. H. Jou and J. J. Shyue, *ACS Nano*, 2010, **4**, 833–840.
7 B. Watts, W. J. Belcher, L. Thomsen, H. Ade and P. C. Dastoor, *Macromolecules*, 2009, **42**, 8392–8397.
8 J. H. Park, J. S. Kim, J. H. Lee, W. H. Lee and K. Cho, *J. Phys. Chem. C*, 2009, **113**, 17579–17584.
9 M. Campoy-Quiles, T. Ferenczi, T. Agostinelli, P. G. Etchegoin, Y. Kim, T. D. Anthopoulos, P. N. Stavrinou, D. D. C. Bradley and J. Nelson, *Nat. Mater.*, 2008, **7**, 158–164.
10 J. Jo, S.-I. Na, S.-S. Kim, T.-W. Lee, Y. Chung, S. J. Kang, D. Vak and D.-Y. Kim, *Adv. Funct. Mater.*, 2009, **19**, 2398–2406.
11 G. Li, Y. Yao, H. Yang, V. Shrotriya, G. Yang and Y. Yang, *Adv. Funct. Mater.*, 2007, **17**, 1636–1644.
12 S. Miller, G. Fanchini, Y.-Y. Lin, C. Li, C.-W. Chen, W.-F. Su and M. Chhowalla, *J. Mater. Chem.*, 2008, **18**, 306–312.
13 M.-S. Su, C.-Y. Kuo, M.-C. Yuan, U.-S. Jeng, C.-J. Su and K.-H. Wei, *Adv. Mater.*, 2011, **23**, 3315–3319.
14 T.-Y. Chu, J. Lu, S. Beaupré, Y. Zhang, J.-R. Pouliot, S. Wakim, J. Zhou, M. Leclerc, Z. Li, J. Ding and Y. Tao, *J. Am. Chem. Soc.*, 2011, **133**, 4250–4253.
15 Y. Liang, Z. Xu, J. Xia, S.-T. Tsai, Y. Wu, G. Li, C. Ray and L. Yu, *Adv. Mater.*, 2010, **22**, E135–E138.
16 Z. He, C. Zhong, S. Su, M. Xu, H. Wu and Y. Cao, *Nat. Photonics*, 2012, **6**, 591–595.
17 S.-Y. Chang, H.-C. Liao, Y.-T. Shao, Y.-M. Sung, S.-H. Hsu, C.-C. Ho and W.-F. Su, *J. Mater. Chem. A*, 2013, **1**, 2447–2452.
18 Y.-C. Huang, G. C. Welch, G. C. Bazan, M. L. Chabinyc and W.-F. Su, *Chem. Commun.*, 2012, **48**, 7250–7252.
19 J. K. Lee, W. L. Ma, C. J. Brabec, J. Yuen, J. S. Moon, J. Y. Kim, K. Lee, G. C. Bazan and A. J. Heeger, *J. Am. Chem. Soc.*, 2008, **130**, 3619–3623.
20 H.-C. Liao, C.-S. Tsao, T.-H. Lin, C.-M. Chuang, C.-Y. Chen, U.-S. Jeng, C.-H. Su, Y.-F. Chen and W.-F. Su, *J. Am. Chem. Soc.*, 2011, **133**, 13064–13073.
21 J. W. Kiel, A. P. R. Eberle and M. E. Mackay, *Phys. Rev. Lett.*, 2010, **105**, 167801-1–167801-4.
22 W.-R. Wu, U.-S. Jeng, C.-J. Su, K.-H. Wei, M.-S. Su, M.-Y. Chiu, C.-Y. Chen, W.-B. Su, C.-H. Su and A.-C. Su, *ACS Nano*, 2011, **5**, 6233–6243.
23 H.-C. Liao, C.-S. Tsao, T.-H. Lin, M.-H. Jao, C.-M. Chuang, S.-Y. Chang, Y.-C. Huang, Y.-T. Shao, C.-Y. Chen, C.-J. Su, U.-S. Jeng, Y.-F. Chen and W.-F. Su, *ACS Nano*, 2012, **6**, 1657–1666.
24 J. Rivnay, S. C. B. Mannsfeld, C. E. Miller, A. Salleo and M. F. Toney, *Chem. Rev.*, 2012, **112**, 5488–5519.
25 W. Chen, T. Xu, F. He, W. Wang, C. Wang, J. Strzalka, Y. Liu, J. Wen, D. J. Miller, J. Chen, K. Hong, L. Yu and S. B. Darling, *Nano Lett.*, 2011, **11**, 3707–3713.
26 W. Chen, M. P. Nikiforov and S. B. Darling, *Energy Environ. Sci.*, 2012, **5**, 8045–8074.
27 M. T. Dang, L. Hirsch, G. Wantz and J. D. Wuest, *Chem. Rev.*, 2013, **113**, 3734–3765.
28 E. Verploegen, C. E. Miller, K. Schmidt, Z. Bao and M. F. Toney, *Chem. Mater.*, 2012, **24**, 3923–3931.
29 Y.-C. Huang, C.-S. Tsao, C.-M. Chuang, C.-H. Lee, F.-H. Hse, H.-C. Cha, C.-Y. Chen, T.-H. Lin, C.-J. Su, U.-S. Jeng and W.-F. Su, *J. Phys. Chem. C*, 2012, **116**, 10238–10244.
30 P. Debye, R. Anderson and H. Brumberger, *J. Appl. Phys.*, 1957, **28**, 679–683.
31 W. L. Griffith, R. Triolo and A. L. Compere, *Phys. Rev. A: At., Mol., Opt. Phys.*, 1987, **35**, 2200–2206.
32 N. D. Treat, M. A. Brady, G. Smith, M. F. Toney, E. J. Kramer, C. J. Hawker and M. L. Chabinyc, *Adv. Energy Mater.*, 2011, **1**, 82–89.
33 E. J. W. Crossland, K. Rahimi, G. Reiter, U. Steiner and S. Ludwigs, *Adv. Funct. Mater.*, 2011, **21**, 518–524.
34 O. Glatter and O. Kratky, *Small-Angle X-Ray Scattering*, Academic Press, London, 1982.
35 D. Credgington, R. Hamilton, P. Atienzar, J. Nelson and J. R. Durrant, *Adv. Funct. Mater.*, 2011, **21**, 2744–2753.